

Quantum Monte Carlo assessment of embedding for a strongly-correlated defect: interplay between mean-field and interactions

Kevin G. Kleiner,¹ Sonali Joshi,¹ Woncheol Lee,² Alexander Hampel,³ Malte Rösner,⁴ Cyrus E. Dreyer,^{3,5} and Lucas K. Wagner¹

¹*Anthony J. Leggett Institute for Condensed Matter Physics,
Department of Physics, Grainger College of Engineering,
University of Illinois at Urbana-Champaign, Urbana, Illinois 61801, USA*

²*Materials Department, University of California, Santa Barbara, California 93106-5050, USA*

³*Center for Computational Quantum Physics, Flatiron Institute,
162 5th Avenue, New York 10010, USA*

⁴*Institute for Molecules and Materials, Radboud University,
Heijendaalseweg 135, 6525 AJ Nijmegen, Netherlands*

⁵*Department of Physics and Astronomy, Stony Brook University, Stony Brook, New York 11794-3800, USA*

(Dated: May 5, 2025)

Point defects are of interest for many applications, from quantum sensing to modifying bulk properties of materials. Because of their localized orbitals, the electronic states are often strongly correlated, which has led to a proliferation of quantum embedding techniques to treat this correlation. In these techniques, a weakly correlated reference such as density functional theory is used to treat most of the one-particle states, while certain states are singled out as an active space to be treated with an effective interaction. We assess these techniques in the context of an iron defect in aluminum nitride by referencing to a fully correlated quantum Monte Carlo description. This comparison allows us to have access to detailed information about the many-body wave functions, which are not available experimentally. We find that errors in the underlying density functional theory calculation, and thus choice of the active space, lead to qualitatively incorrect excited states from the embedded model. These errors are extremely difficult to recover from by adding corrections such as double counting or many-body perturbation theory.

I. INTRODUCTION

Point defects, including impurity atoms, lattice imperfections (i.e., vacancies, interstitials, antisites), and complexes involving the two, profoundly affect the properties of materials. In electronic devices, point defects can be beneficial, e.g., serving as dopants to tune the conductivity of semiconductors over many orders of magnitude, or detrimental, e.g., trapping charge or causing nonradiative recombination [1, 2] in optoelectronic devices. More recently, it has been demonstrated that point defects themselves may serve as quantum devices, including qubits for quantum computing [3, 4], single-photon emitters for quantum communication [5, 6], or nanoprobes for quantum metrology [7]. Recent work has expanded the study of quantum defects to transition metal [8–10] and rare-earth [11–14] impurities. Irrespective of the application, it is crucial to have a quantitative understanding of the defect’s properties and couplings with the host material.

Ab-initio computations have served a key role in developing this understanding, with methods based on density functional theory (DFT) serving as the workhorse [15]. However, it has recently become clear that beyond-DFT methods are required to accurately treat several aspects of point defects, especially those needed for quantum applications. For example, the treatment of electronic excited states [16, 17] is necessary since defect qubit initialization and readout procedures commonly use optical excitations and spin-dependent decay pathways [18, 19]; also, excited state properties play a role in non-radiative

recombination processes at defects [20–22]. Defects may host strongly-correlated electronic states, i.e., those that have multi-reference character, which cannot be treated with DFT [10, 23–25]. This is especially relevant for transition metal or rare-earth impurities with partially-filled d and f orbitals [10, 25].

Quantum embedding methods based on DFT and the constrained random phase approximation (cRPA) have been recently used to address the shortcomings of DFT for defect systems [10, 25–29]. The idea behind these methods is to downfold the full electronic structure of the defect and the host obtained via DFT to a small active space of defect orbitals within which the strongest interactions are assumed to take place. The active space properties are described by an effective Hamiltonian with a one-particle part taken from DFT, and a two-particle screened Coulomb interaction from cRPA [30–34] to explicitly include interactions. Crucially, the one-particle part contains an approximate treatment of the Coulomb interactions inherited from DFT, so a “double counting” (DC) correction is necessary [35, 36]. DFT+cRPA methods have shown considerable promise, e.g., computing excitation energies for the negatively-charged nitrogen-vacancy (NV^-) center in diamond and the neutrally-charged silicon-vacancy center in diamond to within a few tenths of an eV from experiment [25, 27–29].

The key challenge for defect embedding methods is that there are several uncontrolled approximations made when deriving effective Hamiltonians. As mentioned above, an approximate DC correction must be chosen,

since it is not possible to determine exactly the DFT Coulomb interaction in the active space. Significant progress in this direction has been made by instead using G_0W_0 as a starting point for the embedding, in which case the self-energy may be straightforwardly decomposed into contribution inside and outside of the active space [37]. The use of G_0W_0 also, to some extent reduces the dependence on the DFT functional for the initial calculation [37], though this is expected to be system dependent. In addition, depending on the system, the initial electronic configuration used for the DFT or G_0W_0 calculation may be ambiguous. For example, it is common in embedding methods to use a spin-unpolarized starting point for the mean-field method, since exchange interactions are explicitly included in the two-particle part; however, the spin-unpolarized electronic structure may be very different than the spin-polarized one. Finally, treating the screening at the RPA level is an approximation to be tested [29, 38].

However, embedding results may depend qualitatively on the choices made for the above approximations, especially for strongly correlated defects. For example, DFT+cRPA with a DC correction neglecting exchange-correlation effects led to an incorrect low-spin ground state for a neutrally-charged iron substitutional impurity in aluminum nitride ($Fe_{Al}^0:AlN$) [25]. The G_0W_0 -based scheme of Ref. [37], on the other hand, gave the correct ground state for $Fe_{Al}^0:AlN$ and lowest excited states within 0.5 eV from experiment [10]. The choice of active space orbitals, assumption of static screening in cRPA, and DC correction have each been shown to change the computed excitation energies by at least 0.5 eV for a vanadocene molecule [39], which can be considered a model of a strongly correlated defect.

In contrast to embedding methods, *ab-initio* quantum Monte Carlo (QMC) methods provide a full many-body wave-function treatment of interactions in defect systems [40]. QMC methods have been commonly used to compute ground state properties of defect systems, including formation energies of Schottky defects in magnesium oxide [41], self-interstitials in silicon [42], helium in aluminum [43], oxygen-vacancies in magnesium oxide [44], and nitrogen in zinc oxide [45]. The extension of QMC to defect excited states is still relatively new, currently including neutrally-charged vacancy centers in diamond [46], magnanese dopants in phosphors [47], and the NV^- center in diamond [48, 49]. More recently, some of us introduced an explicit variational principle for excited states in Ref. [50], offering a means to systematically improve excited state wave functions.

In this work, we compare vertical excitations from embedding methods against well-controlled *ab-initio* QMC calculations for a small unit cell of $Fe_{Al}^0:AlN$. By comparing the embedding and QMC methods on the same system, the computed spectra should differ only because of errors in the methods. To obtain the QMC reference, we optimize the trial wave functions using the excited state variational principle discussed in Ref. [50]. We then

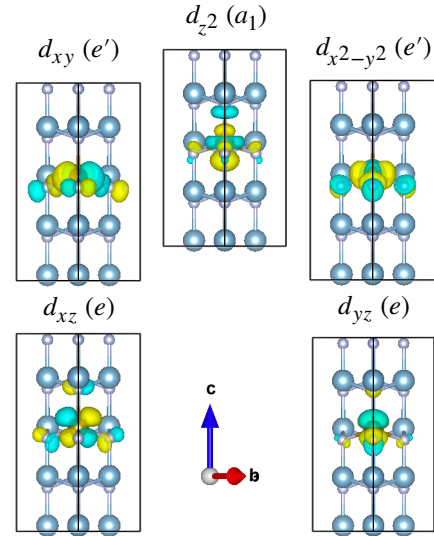


FIG. 1. **Reference atomic d -like orbitals used for the analysis of $Fe_{Al}^0:AlN$ defect states.** Each orbital is labeled by cubic harmonic character with corresponding irreducible representation of the C_{3v} point group, consisting of an e -orbital pair, an e' orbital pair, and an a_1 orbital. Crystallographic vectors \mathbf{a} , \mathbf{b} , and \mathbf{c} are labeled in the center, with \mathbf{a} pointing into the page. Large blue atoms are Al, small grey atoms are N, and the large orange atom is Fe.

determine whether embedding methods obtain excited states consistent with QMC, with respect to excitation energies and Fe d orbital occupations. The occupations allow for an additional confirmation that the character of the wave functions also match between methods, and thus the agreement of energies is not just fortuitous. As we will see, several standard embedding methods obtain lowest excited states with excitation energies a few tenths of an eV from QMC, but with different orbital character.

The rest of the manuscript is organized as follows. In Sec. II, we introduce the $Fe_{Al}^0:AlN$ benchmark system and its electronic structure. In Sec. III, we explain the *ab-initio* QMC and defect embedding methods including calculation details. In Sec. IV, we determine the QMC reference and compare the vertical excitation energy results between embedding methods and QMC. In Sec. V, we conclude the paper.

II. BENCHMARK SYSTEM

For the benchmark system, we chose a 32-atom unit cell of $Fe_{Al}^0:AlN$ with one defect in its ground state equilibrium geometry. The $Fe_{Al}^0:AlN$ structure has C_{3v} symmetry with three-fold rotation about the crystallographic c -axis and mirror reflection about the (110) plane [21, 22, 25]. The four Fe-N bonds form a quasi-tetrahedron with one bond roughly 0.5% longer than the other three bonds. Hence, the defect structure has close

to T_d (tetrahedral) symmetry.

At the spin-unpolarized DFT level [21, 22, 25], the system has Fe d -like orbitals in the band gap, occupied by five electrons. Based on the C_{3v} crystal field splitting, the single-particle states form a doubly-degenerate e orbital pair arising from d_{xy} and d_{xz} , doubly-degenerate e' orbital pair arising from $d_{x^2-y^2}$ and d_{yz} , and non-degenerate a_1 orbital arising from d_{z^2} , as shown in Fig. 1 and labeled using irreducible representations (irreps) of C_{3v} . The a_1 and e' orbitals would form the triply-degenerate t_{2g} manifold if the site symmetry were T_d . The five d -like orbitals have small lobes around the N sites neighboring the Fe site, indicating finite hybridization with N p orbitals. We note that this spin-unpolarized DFT electronic structure is very different from the spin-polarized DFT picture [22], where the filled majority spin Fe d bands split from the empty minority spin ones by ~ 10 eV, the former ending up below the N p valence band manifold and the latter above the conduction-band minimum. Thus, $\text{Fe}_\text{Al}^0:\text{AlN}$ is a case where the validity of the spinless DFT starting point must be confirmed.

From the site symmetry and d occupation of the Fe impurity, we can determine the expected many-body states from ligand field theory [51]. For a free Fe^{3+} ion, the ground state is the spin-5/2 six-fold degenerate 6S manifold, while the first excited state is the spin-3/2 36-fold degenerate 4G manifold. For a relatively small T_d crystal field splitting (CFS) relative to the Racah interaction parameter B , the ground state remains six-fold degenerate, now referred to as 6A_1 . With increasing T_d CFS, the 4G manifold splits into 4T_1 , 4T_2 , and $^4E + ^4A_1$ [51], listed in order of increasing many-body energies. Lowering the site symmetry from T_d to C_{3v} , the 4T_1 manifold further splits into 4A_2 and 4E , and the 4T_2 manifold further splits into 4A_1 and 4E . Low-spin states from the 2I manifold of the free ion may also mix with the spin-quadruplet states for larger CFS/B; in fact, 2T_2 becomes the ground state for large CFS/B. However, experimental measurements for $\text{Fe}_\text{Al}^0:\text{AlN}$ [52, 53] support the low-CFS picture with a high-spin ground state. We will see the QMC calculations also obtain a high-spin ground state.

III. METHODS

A. Geometry relaxation

To obtain the ground state equilibrium geometry for $\text{Fe}_\text{Al}^0:\text{AlN}$, we generated a 2x2x2 supercell of wurtzite AlN using the primitive cell on the Materials Project database [54], substituted an Fe atom for an Al atom, and relaxing the geometry at the spin-unpolarized DFT level. We use the VASP [55] code with the Perdew-Burke-Ernzerhof (PBE) exchange-correlation functional [56], an energy cutoff for the plane-wave basis of 500 eV, projector-augmented wave pseudo-potentials, 2x2x2 k-space mesh, and Gaussian thermal smearing with width $\sigma = 0.01$ eV.

B. *Ab-initio* QMC methods

To obtain QMC estimates for the *ab-initio* ground state and low-lying vertical excitations of $\text{Fe}_\text{Al}^0:\text{AlN}$, we constructed trial wave functions in multi-Slater-Jastrow form,

$$\Psi(\mathbf{R}) = e^{J(\mathbf{R})} \sum_k c_k D_k^\uparrow(\mathbf{R}) D_k^\downarrow(\mathbf{R}), \quad (1)$$

where \mathbf{R} encompasses the coordinates for all 141 electrons in the system, e^J is a Jastrow factor, and $\sum_k c_k D_k^\uparrow D_k^\downarrow$ is a linear expansion of Slater determinants built from occupied one-particle spin-up and spin-down orbitals. The one-particle orbitals were generated from spin-restricted open-shell DFT calculations in PySCF [57] for a $S_z = +5/2$ reference state, using correlation-consistent pseudo-potentials [58], atom-centered Gaussian basis functions with decay exponents above 0.1, and a 1x1x1 k-mesh. The multi-Slater expansions were generated from a complete active space configuration interaction (CASCI) calculation in PySCF, using an active space of three spin-up and two spin-down electrons in the five Fe d -like DFT orbitals. We append the same two-body Jastrow function [59] for all eigenstates, optimized using variational Monte Carlo methods for the ground state in PyQMC [60]. The fixed Jastrow lowers the lowest vertical excitation energies by roughly 1 eV (see Sec. VII A).

We systematically improved the trial wave functions for the eigenstates using the recently-introduced ensemble variational principle with cost functional [50]

$$C[\Psi_1, \Psi_2, \dots] = \sum_i w_i E[\Psi_i] + \lambda \sum_{i < j} |\langle \Psi_i | \Psi_j \rangle|^2, \quad (2)$$

where $\sum_i w_i E[\Psi_i]$ is a weighted sum of the states' total energies and λ is a penalty on the states' mutual overlaps. Ref. [50] proved Eq. (2) is minimized at the eigenstates when setting decreasing weights $w_1 > w_2 > \dots$ and λ larger than a threshold value. We optimized the cost for the lowest fifteen states with respect to the DFT functional and basis set used for the one-particle orbitals, including the PBE and Heyd-Scuseria-Ernzerhof (HSE06) functionals [61, 62] and vtz and vqz Gaussian basis sets.

For each *ab-initio* eigenstate, we computed the total energy, one- and two-particle density matrices in the Fe d -like DFT orbitals, and expectation values of C_{3v} symmetry operators with variational Monte Carlo. To remove arbitrary rotations of the d -like orbitals in DFT, we rotated the density matrices into the intrinsic atomic orbital (IAO) basis [63], as shown in Fig. 1. We obtained orbital occupations using the diagonal entries of the one-particle density matrices. We determined an irrep for each state using the two-particle density matrices and symmetry expectation values (see Sec. VII B).

C. Defect embedding methods

In embedding methods for $\text{Fe}_{\text{Al}}^0:\text{AlN}$, we derived Hamiltonians of the form

$$\hat{H}_{\text{eff}} = \sum_{i,j \in \text{Fe}_d} \sum_{\sigma \in \{\uparrow, \downarrow\}} t_{ij} (\hat{c}_{i,\sigma}^\dagger \hat{c}_{j,\sigma} + h.c.) + \frac{1}{2} \sum_{i,j,k,l \in \text{Fe}_d} \sum_{\sigma, \sigma' \in \{\uparrow, \downarrow\}} U_{ijkl} \hat{c}_{i,\sigma}^\dagger \hat{c}_{j,\sigma} \hat{c}_{k,\sigma'}^\dagger \hat{c}_{l,\sigma'} - \hat{H}_{\text{DC}}, \quad (3)$$

where σ, σ' indicate spin-up or spin-down and i, j, k, l indicate the d -like orbitals shown in Fig. 1, t_{ij} are one-particle hoppings, U_{ijkl} are two-particle interactions in chemistry ordering, and \hat{H}_{DC} is the DC correction.

DFT+cRPA methods require a self-consistent DFT calculation for the Kohn-Sham density, followed by a non-self-consistent DFT calculation for the active space orbitals and one-particle hoppings, followed by a cRPA calculation for the screened two-particle interactions in the active space, followed by adding a DC correction. The Kohn-Sham densities were computed with spin-unpolarized DFT in **Quantum Espresso** [64], using the PBE functional, plane wave basis with energy cutoff of 5850 eV, correlation-consistent pseudo-potentials consistent with the QMC, 4x4x2 k-space mesh, and Gaussian thermal smearing with width $\sigma = 1.36 \cdot 10^{-7}$ eV. The Fe d -like active space orbitals and hoppings were computed with the same settings, except without self-consistency and using a 1x1x1 k-mesh. To simplify the cRPA calculations, we rotated the five active space orbitals into d -like projected Wannier functions in the **pw2wannier90** interface to **Wannier90** [65]. The screened interactions were computed in the Wannier basis using static limit cRPA with 22 bands/atom with the **wan2respack** interface to **RESPACK** [66, 67].

We tested the dependence of the DFT+cRPA results on the DFT reference state and on the choice of DC correction. The reference states involved different occupations of the spin-unpolarized Fe d -like one-particle states. In our DFT calculations, the states were ordered in energy as e, a_1 , and e' . We note the a_1 , and e' states switch ordering in larger supercells [22, 25]. We chose two target states $|22100\rangle$ and $|11111\rangle$, labeling by their total occupations in the five Fe d -like DFT orbitals. $|22100\rangle$ is the lowest energy state in spin-unpolarized DFT. Both states preserve the C_{3v} symmetry of the defect.

For the DC correction, we considered three cases. The first is neglecting the correction altogether. At first sight, this seems to be the least rigorous approach; however, it is important to note that in our context, this follows the approach taken by most DFT-based embedding methods. The reason is because we are only considering transitions between states in the active space, and the conventional use of the DC correction is to correct the energy spacing between the active space and bulk orbitals. In our case, the reason DC makes a difference to the active-space spectra is because we are explicitly including *orbital dependence*, which is usually neglected [35].

The second form of the DC we consider is the approximation that the DFT treatment of the Coulomb interaction is described at the Hartree level, but with the cRPA screened interaction [25–27]. The Hartree DC correction has the form

$$\hat{H}_{\text{DC}}^{\text{Hartree}} = \sum_{i,j \in \text{Fe}_d} \sum_{\sigma \in \{\uparrow, \downarrow\}} \left(\sum_{k,l \in \text{Fe}_d} \rho_{kl} U_{ijkl} \right) \hat{c}_{i,\sigma}^\dagger \hat{c}_{j,\sigma}, \quad (4)$$

where ρ_{kl} is the one-particle density matrix in the DFT reference state.

For the third form, we utilize the G_0W_0 -based embedding method of Ref. 37. This method requires a G_0W_0 calculation to be performed on the defect supercell after the initial DFT. There are two equivalent ways to think about this method. It can be considered as an “exact” way to include the exchange-correlation contribution in the active space to the DC, i.e., by replacing the exchange-correlation potential by the G_0W_0 self energy, and then removing the contribution in the active space; the other is simply that the DFT mean-field starting point is replaced by G_0W_0 . G_0W_0 -based embedding derives a one-particle Hamiltonian of the form

$$\hat{H}_{G_0W_0} = (\hat{H}_{\text{KS}} - iG_0W_0) - (\hat{H}_{\text{DC}}^{\text{Hartree}} - iG_0^A W_0), \quad (5)$$

where \hat{H}_{KS} is the Kohn-Sham Hamiltonian in the active space, G_0 is the bare one-particle Green function, G_0^A the Green function in the active space, and W_0 is the fully-screened Coulomb interaction in the active space. The first two terms are the G_0W_0 band structure and the last two terms are the G_0W_0 DC correction. Using the DFT eigenvalues and RPA screening, we obtained G_0W_0 one-particle energies and DC corrections with the **pw2bgw** interface to **BerkeleyGW** [68, 69]. The two-particle interactions in the G_0W_0 model are identical to those in DFT+cRPA.

To ensure comparable orbital occupations between the states from DFT+cRPA and QMC, we rotated the final embedding models from the Wannier basis sets into the reference IAO basis, as shown in Fig. 1. The orbital transformations are nearly one-to-one (see Sec. VII C). After rotating, we checked the resulting models’ invariance to C_{3v} symmetry operations in the IAO basis. We then obtained the models’ eigenstates using exact diagonalization in **PySCF**.

IV. RESULTS AND DISCUSSION

A. Reference defect states from QMC

We investigated dependence of the $\text{Fe}_{\text{Al}}^0:\text{AlN}$ eigenstates on one-particle orbitals used in the multi-Slater-Jastrow wave function *ansatz*, shown in Fig. 2. The orbitals come from DFT with the PBE and HSE06 func-

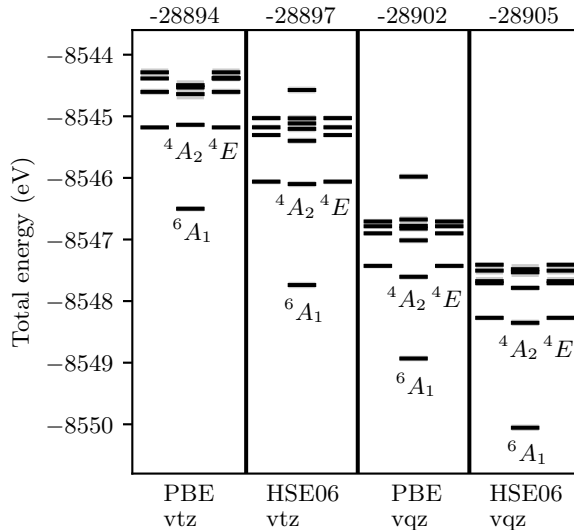


FIG. 2. Variational optimization of QMC-computed eigenstates for $\text{Fe}_{\text{Al}}^0:\text{AlN}$ using multi-Slater-Jastrow *ansätze*, ordered by decreasing ensemble cost. The columns correspond to mean-field functional and basis set used for the orbitals in the wave functions, with ensemble cost in eV units shown along the top. Single- σ statistical errors on the energies are shown as lightly-shaded boxes. The lowest few eigenstates are labeled according to spin degeneracy and many-particle irrep of C_{3v} , using capital letters to distinguish from the one-particle irreps shown in Fig. 1. Doubly-degenerate E states are horizontally displaced for clarity.

tionals and with vtz and vqz Gaussian basis sets. Irrespective of functional and basis set, the ground state has 6A_1 symmetry and lowest three excited states have 4A_2 and 4E symmetries, exactly in line with the ligand-field theory expectations [51].

To estimate uncertainty in the QMC results, we compared the QMC-computed 4A_2 vertical excitation energy for the different *ansätze* in Table I. The two DFT functionals lead to the same excitation energy within single- σ statistical error bars. The larger vqz basis set leads to an excitation energy larger by several σ than when using vtz.

We determined the one-particle orbitals for the multi-Slater-Jastrow wave functions by minimizing the ensemble cost functional defined in Eq. (2) [50]. The HSE06 vqz orbitals lead to minimal ensemble cost for the lowest fifteen states, as shown in Fig. 2. Hence, we selected the wave functions with HSE06 vqz orbitals for the QMC reference.

To gain further confidence in the QMC results, we can compare to available experimental data. We note that the goal of these calculations was not to match experiment, but to provide a consistent comparison with the quantum embedding. Indeed, the small supercell size that we use is likely a source of finite-size error. However, the results are in excellent qualitative agreement with experiment. The QMC ground state symmetry co-

TABLE I. Comparison of 4A_2 vertical excitation energies from each QMC calculation for $\text{Fe}_{\text{Al}}^0:\text{AlN}$. The QMC energies are listed in order of multi-Slater-Jastrow wave functions with decreasing ensemble cost, as shown in Fig. 2.

	Excitation energy (eV)
PBE vtz	1.36(6)
HSE06 vtz	1.33(7)
PBE vqz	1.64(8)
HSE06 vqz	1.70(9)

incides with the 6A_1 ground state observed in emission Mössbauer spectroscopy measurements [52]. For the excited states, photoluminescence studies report the zero-phonon-line (ZPL) energy of the $^4E-^6A_1$ transition at 1.30 eV [70]. In this work, we focus on *vertical* excitation energies. The vertical excitation energy of absorption is related to the ZPL energy through subtracting the excited state lattice relaxation energy and the difference in zero-point vibrational energies between the two states. Ref. [10] reports a 0.11 eV lattice relaxation energy in the 4E excited state, as computed at the spin-flip time-dependent density functional theory level for a 256-atom cell. They also assume cancellation of zero-point vibrational energies, which was shown to be a valid approximation for defects in Ref. [53]. Hence, using the relaxation energy from Ref. [10] and the experimental ZPL we estimate a vertical energy of ~ 1.41 eV. As can be seen in Table I, the QMC best-estimate of 1.70(6) eV is within 0.4 eV of this value; we consider this quite good agreement in light of the expected finite-size effects. Errors of a few tenths of an eV are common for excited state calculations of transition metal systems with state-of-the-art correlated electron methods [39].

In summary, we obtained variational best estimates for the lowest fifteen eigenstates of $\text{Fe}_{\text{Al}}^0:\text{AlN}$ when using multi-Slater-Jastrow wave functions with HSE06 vqz mean-field orbitals. We now proceed to compare these with results with the results of the quantum embedding methodology discussed in Sec. III C.

B. Comparison to defect embedding methods

In contrast to QMC, DFT+cRPA methods require the user to make several choices such as the one-particle reference state in DFT, screening model for cRPA, and DC correction. G_0W_0 -based methods seek to remove some of the approximations present in DFT+cRPA with one-particle energies based on G_0W_0 and an exact DC correction [37]. Here, we investigated which approximations in embedding most affect the computed vertical excitation energies as compared to QMC calculations for the same Hamiltonian.

The results for the embedding calculations for the ground and low-lying excited states of $\text{Fe}_{\text{Al}}^0:\text{AlN}$ are given in the first five panels of Fig. 3; each involves a different

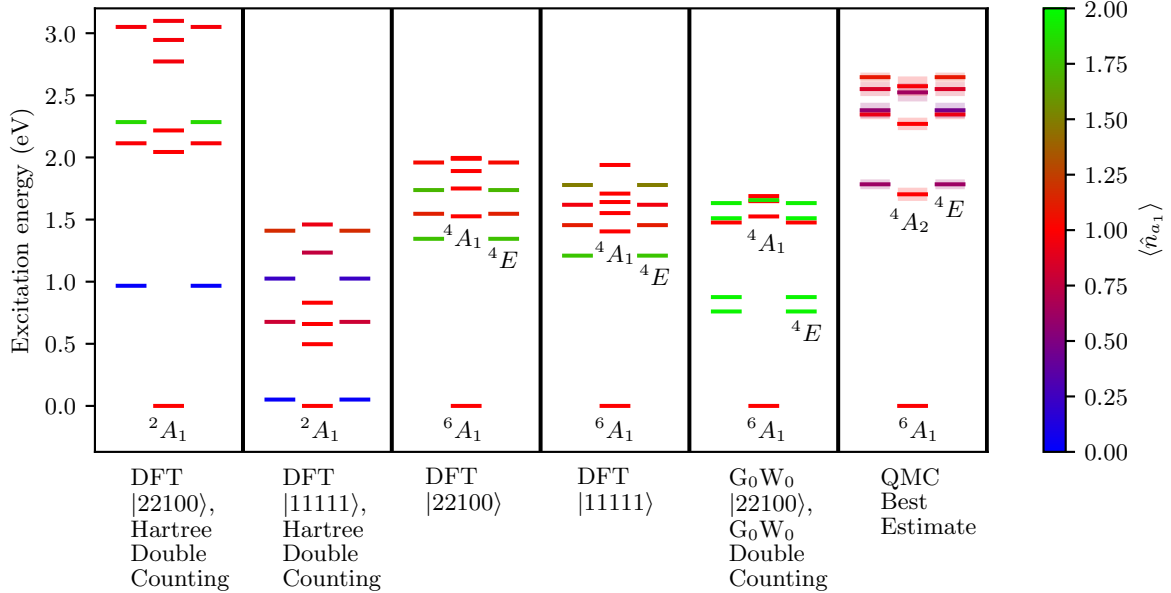


FIG. 3. DFT+cRPA without DC correction obtains 4E lowest excited states with different orbital character than those of QMC, despite having excitation energies agreeing to QMC within uncertainties. G_0W_0 -based embedding doesn't improve the agreement to QMC. From left to right, the columns correspond to DFT+cRPA with $|22100\rangle$ and $|11111\rangle$ reference states and Hartree DC correction, DFT+cRPA with $|22100\rangle$ and $|11111\rangle$ reference states and no DC correction, G_0W_0 -based embedding with the $|22100\rangle$ reference state and G_0W_0 DC correction, and the best-estimate QMC reference. The DFT reference states are labeled using occupation constraints in the five Fe d -like Kohn-Sham orbitals. The energy levels are colored by a_1 orbital occupation, computed in the basis of the HSE06 vqz orbitals.

choice for the DC correction and initial DFT occupancies. For comparison, our QMC best estimate (i.e., using HSE06 vqz orbitals) is given in the sixth panel.

In Ref. [25], some of us showed that DFT+cRPA with no DC correction obtains a many-body ground state and lowest excited states in qualitative agreement with experiment. We give these results for the 32-atom cell in the third and fourth panel of Fig. 3. At first sight, the qualitative features are somewhat similar to the QMC. The ground state has 6A_1 symmetry, and the lowest spin-quadruplet excited states are ~ 1.3 eV above the ground state. However, we do see that the lowest excited states are 4E and 4A_1 , as compared to 4E and 4A_2 in QMC. We also find that the orbital character of the states are different. In particular, the a_1 orbital is doubly occupied in the 4E lowest excited states from the embedding model, while it is less than singly occupied in QMC.

We find that the Hartree DC correction defined in Eq. (4) most affects the computed spectrum for this system, as was noted in Ref. [25]. The Hartree DC correction results in an incorrect 2A_1 ground state, in contrast to the 6A_1 ground state from QMC, regardless of the one-particle reference state. We can see why by analyzing the one-particle energies in the IAO basis, as shown in Table II. The Hartree DC corrections decrease the e orbital energies by roughly 1.5 eV more than the a_1 and e' and orbital energies. The e orbital energies shift the most because the Fe d_{xz} and d_{yz} orbitals hybridize the least

with the neighboring N p orbitals, resulting the higher localization shown in Fig. 1, which then results in a larger Hartree energy and DC correction. The enlarged one-particle splittings in the model ultimately lead to the low-spin ground states shown in Fig. 3. Thus, DC in DFT+cRPA likely has a large cancellation of Hartree and exchange-correlation terms for $Fe_{Al}^0:AlN$, a system where orbital localization varies among the d orbitals in the active space.

Given the importance of beyond-Hartree DC corrections for $Fe_{Al}^0:AlN$, one hypothesis is that G_0W_0 -based embedding with exact G_0W_0 DC correction leads to better results, as discussed in Ref. [10]. We find that not to be the case, though the results are qualitatively much more similar to DFT+cRPA without DC corrections than with the Hartree DC correction. As can be seen in Fig. 3, the G_0W_0 model obtains the correct ground state in agreement with the results in Ref. [10]. However, the 4E lowest excited states have excitation energy roughly 1 eV lower than QMC and a doubly-occupied a_1 orbital, in contradiction to the QMC-computed first excited states. The spectrum also contains two sets of doubly degenerate 4E excited states at low energy, as opposed to the quasi-triply degenerate lowest excited states from the DFT+cRPA models and QMC. Thus, DC is not the only major source of error in embedding methods for this system.

C. Analyzing failure modes of defect embedding

We now analyze the sources of discrepancy between the the QMC and embedding methods. Some insight into the G_0W_0 results can be obtained by examining the one-particle energies in Table II. Since the defect has nearly T_d symmetry, one would expect the d orbitals to be split into two degenerate e_g states at lower energy and three quasi-triply degenerate t_{2g} states at higher energy. Indeed, the DFT+cRPA methods result in this pattern, with a small 0.1 eV splitting of the t_{2g} orbitals. However, the G_0W_0 one-particle energies after DC correction reverse this pattern, with three nearly degenerate orbitals at lower energy and two at higher energy. This results from a large 2 eV T_d CFS from G_0W_0 combined with an even larger correction from the G_0W_0 DC terms. The reversal of T_d ordering ultimately leads to the two sets of low-lying 4E excited states, as can be seen in Fig. 3.

An interesting similarity between the G_0W_0 and DFT+cRPA with no DC correction is the near double occupancy in a_1 in the lowest-energy 4E states, in contrast to QMC where occupancy is ~ 0.5 electrons. To gain insight into the physics, we can again turn to ligand field theory (see Sec. VII D). In this case, we assume a spherically symmetric form of the screened Coulomb interaction, and a one-particle part that enforces the C_{3v} CFS. We see that for the range of CFS parameters relevant for $Fe_{Al}^0:AlN$, we find that the lowest-lying 4E states have an a_1 occupancy of 0.5 – 0.7 electrons, while 4A_2 has an a_1 occupancy of 1 electron. We see that this is exactly what is obtained by the QMC. This means that the QMC is indicating a significantly more spherically-symmetric Coulomb interaction that is found by cRPA.

We can quantify the overestimation of the non-spherical interactions using the QMC-computed energies and a_1 orbital occupations. In particular, none of the QMC-computed excited states with energies below 3 eV doubly occupy the a_1 orbital, as can be seen from Fig. 3. One can infer double occupancies in the a_1 orbital are penalized significantly less in energy by the embedding models than by the *ab-initio* model. We can see why by analyzing the on-site interactions in the IAO basis, as shown in Table III. Both with and without cRPA screening, the interaction in the a_1 orbital is significantly smaller than in the e and e' orbital. In the spherically symmetric case, all diagonal elements are equal, so this deviation is a result of the non-spherical symmetry of the Coulomb interaction from cRPA. Since the large deviation is already showing up in the bare Coulomb matrix elements, a likely contributor is an overly delocalized a_1 orbital from DFT relative to e and e' .

We note that this over-delocalization of the DFT defect orbitals is exacerbated by the small simulation cell. Indeed, performing DFT+cRPA in a larger cell results in a more spherically-symmetric Coulomb interaction. For example, the difference in cRPA-screened $U_{e'}$ and U_{a_1} reduces to 0.04 eV for a 72-atom cell, relative to the 0.34 eV difference for the 32-atom cell shown in Table III. The re-

TABLE II. Comparison of one-particle energies relative to ϵ_{a_1} and hoppings in the reference IAO basis across the embedding models.

	ϵ_e (eV)	ϵ_{a_1} (eV)	$\epsilon_{e'}$ (eV)	$t_{ee'}$ (eV)
DFT $ 22100\rangle$, Hartree Double Counting	-2.45	0	-0.01	-1.84
DFT $ 11111\rangle$, Hartree Double Counting	-2.08	0	-0.73	-1.19
DFT $ 22100\rangle$	-0.59	0	0	-0.49
DFT $ 11111\rangle$	-0.69	0	0	-0.56
G_0W_0 $ 22100\rangle$	-2.01	0	-0.29	-1.43
G_0W_0 $ 22100\rangle$, G_0W_0 Double Counting	0.23	0	0.79	-0.29

TABLE III. Comparison of bare and screened two-particle interactions in the reference IAO basis. The bare and screened interactions both use orbitals from DFT with the $|22100\rangle$ reference state.

	U_e (eV)	U_{a_1} (eV)	$U_{e'}$ (eV)
Bare	16.81	13.34	14.24
Screened	3.08	2.35	2.69

sulting lowest 4E excited states from DFT+cRPA have nearly singly-occupied a_1 orbital for the 72-atom cell, which is a significant qualitative change relative to the 32-atom case shown in Fig. 3. The fact that QMC finds such behavior in the 32-atom cell suggests that cRPA is not able to correct for the over-delocalization of DFT orbitals for $Fe_{Al}^0:AlN$, a system with significant hybridization between the defect and the bulk states at the DFT level.

V. CONCLUSION

We have performed a detailed comparison between quantum Monte Carlo (QMC) and quantum embedding for a substitutional Fe impurity in AlN. Using a small 32-atom supercell allowed us to make a consistent comparison between embedding techniques and high-level many-body wave function solutions to the correlated-electron problem. We compared the computed excitation energies and wave function properties between embedding methods using different choices of approximations and the reference QMC results.

These choices included the initial density functional theory (DFT) configuration used for the one-particle part of the embedding Hamiltonian and the double counting correction. As has been demonstrated previously [25, 26, 37], we find the double-counting correction plays a significant role in the spectra of many-body states. Though several choices provide qualitatively similar spectra to QMC, the precise ordering in terms of state symmetries and orbital character is not well-reproduced by any of them. We note that the low-lying excited states

also do not follow the predictions of ligand-field theory, while QMC does.

We identify the following failure modes of the quantum embedding. First, the T_d -to- C_{3v} crystal field splitting appears to be overestimated by DFT in the one-particle part of the Hamiltonian, and this is not effectively corrected by Hartree double counting approximation. The Hartree double counting correction incorrectly lowers the relative energy of e orbitals because of differing orbital localizations in the active space. For the G_0W_0 -based embedding method with exact G_0W_0 double counting correction [37], the one-particle energies are inverted from what one would expect from a near- T_d system, i.e., the quasi- t_{2g} orbitals are below the e_g orbitals. Also, the deviations from ligand field theory suggest overestimated non-spherical contributions to the two-particle interaction tensor.

This work demonstrates the utility of comparing high-accuracy *ab-initio* many-body calculations to quantum embedding results for small systems to determine the accuracy of approximations. It also provides a cautionary example of how many-body spectra may be insufficient for benchmarking, and additional parameters (e.g., the orbital character in the excited states) should be compared. These aspects will be crucial to developing the

promise of quantum embedding as an accurate and efficient computational method for strongly correlated point defects.

VI. ACKNOWLEDGEMENTS

CED thanks Coraline Letouzé for fruitful conversations. KGK acknowledges support from the National Science Foundation under Award No. DGE-1922758 and the Graduate Research Fellowship Program under Grant No. DGE-1746047. CED acknowledges support from the NSF under Award No. DMR-2237674. LKW and SJ acknowledge support from the U.S. Department of Energy, Office of Science, Office of Basic Energy Sciences, Computational Materials Sciences Program, under Award No. DE-SC0020177. KGK and WL acknowledge support from the Flatiron Institute's Center for Computational Quantum Physics pre-doctoral program. The QMC and embedding calculations used supercomputing resources from the Flatiron Institute's Scientific Computing Core. The Flatiron Institute is a division of the Simons Foundation.

[1] W. Shockley and W. T. Read, Statistics of the Recombinations of Holes and Electrons, *Physical Review* **87**, 835 (1952).

[2] R. N. Hall, Electron-Hole Recombination in Germanium, *Physical Review* **87**, 387 (1952).

[3] J. R. Weber, W. F. Koehl, J. B. Varley, A. Janotti, B. B. Buckley, C. G. Van De Walle, and D. D. Awschalom, Quantum computing with defects, *Proceedings of the National Academy of Sciences* **107**, 8513 (2010).

[4] B. E. Kane, A silicon-based nuclear spin quantum computer, *Nature* **393**, 133 (1998).

[5] I. Aharonovich, S. Castelletto, D. A. Simpson, C.-H. Su, A. D. Greentree, and S. Prawer, Diamond-based single-photon emitters, *Reports on Progress in Physics* **74**, 076501 (2011).

[6] I. Aharonovich, D. Englund, and M. Toth, Solid-state single-photon emitters, *Nature Photonics* **10**, 631 (2016).

[7] R. Schirhagl, K. Chang, M. Loretz, and C. L. Degen, Nitrogen-Vacancy Centers in Diamond: Nanoscale Sensors for Physics and Biology, *Annual Review of Physical Chemistry* **65**, 83 (2014).

[8] L. Shang, Q. Chen, W. Jing, C.-G. Ma, C.-K. Duan, and J. Du, First-principles study of transition metal dopants as spin qubits, *Physical Review Materials* **6**, 086201 (2022).

[9] C.-W. Lee, M. Singh, A. C. Tamboli, and V. Stevanović, Transition metal impurities in silicon: Computational search for a semiconductor qubit, *npj Computational Materials* **8**, 172 (2022).

[10] L. Otis, Y. Jin, V. W.-z. Yu, S. Chen, L. Gagliardi, and G. Galli, Strongly correlated states of transition metal spin defects: The case of an iron impurity in aluminum nitride (2025), [arXiv:2501.16280 \[cond-mat\]](https://arxiv.org/abs/2501.16280).

[11] A. I. Lvovsky, B. C. Sanders, and W. Tittel, Optical quantum memory, *Nature Photonics* **3**, 706 (2009).

[12] R. Kolesov, K. Xia, R. Reuter, R. Stöhr, A. Zappe, J. Meijer, P. Hemmer, and J. Wrachtrup, Optical detection of a single rare-earth ion in a crystal, *Nature Communications* **3**, 1029 (2012).

[13] D. D. Awschalom, R. Hanson, J. Wrachtrup, and B. B. Zhou, Quantum technologies with optically interfaced solid-state spins, *Nature Photonics* **12**, 516 (2018).

[14] J. Zhang, G. D. Grant, I. Masiulionis, M. T. Solomon, J. C. Marcks, J. K. Bindra, J. Niklas, A. M. Dibos, O. G. Poluektov, F. J. Heremans, S. Guha, and D. D. Awschalom, Optical and spin coherence of Er spin qubits in epitaxial cerium dioxide on silicon, *npj Quantum Information* **10**, 119 (2024).

[15] C. Freysoldt, B. Grabowski, T. Hickel, J. Neugebauer, G. Kresse, A. Janotti, and C. G. Van De Walle, First-principles calculations for point defects in solids, *Reviews of Modern Physics* **86**, 253 (2014).

[16] P. Mori-Sánchez, A. J. Cohen, and W. Yang, Many-electron self-interaction error in approximate density functionals, *The Journal of Chemical Physics* **125**, 201102 (2006).

[17] Y. Ma, M. Rohlfing, and A. Gali, Excited states of the negatively charged nitrogen-vacancy color center in diamond, *Physical Review B* **81**, 041204 (2010).

[18] M. W. Doherty, N. B. Manson, P. Delaney, F. Jelezko, J. Wrachtrup, and L. C. Hollenberg, The nitrogen-vacancy colour centre in diamond, *Physics Reports* **528**, 1 (2013).

[19] M. L. Goldman, M. W. Doherty, A. Sipahigil, N. Y. Yao, S. D. Bennett, N. B. Manson, A. Kubanek, and M. D. Lukin, State-selective intersystem crossing in nitrogen-vacancy centers, *Physical Review B* **91**, 165201 (2015).

[20] A. Alkauskas, C. E. Dreyer, J. L. Lyons, and C. G. Van De Walle, Role of excited states in Shockley-Read-Hall recombination in wide-band-gap semiconductors, *Physical Review B* **93**, 201304 (2016).

[21] D. Wickramaratne, J.-X. Shen, C. E. Dreyer, M. Engel, M. Marsman, G. Kresse, S. Marcinkevičius, A. Alkauskas, and C. G. Van De Walle, Iron as a source of efficient Shockley-Read-Hall recombination in GaN, *Applied Physics Letters* **109**, 162107 (2016).

[22] D. Wickramaratne, J.-X. Shen, C. E. Dreyer, A. Alkauskas, and C. G. Van De Walle, Electrical and optical properties of iron in GaN, AlN, and InN, *Physical Review B* **99**, 205202 (2019).

[23] U. Von Barth, Local-density theory of multiplet structure, *Physical Review A* **20**, 1693 (1979).

[24] J. Lischner, J. Deslippe, M. Jain, and S. G. Louie, First-Principles Calculations of Quasiparticle Excitations of Open-Shell Condensed Matter Systems, *Physical Review Letters* **109**, 036406 (2012).

[25] L. Muechler, D. I. Badrtdinov, A. Hampel, J. Cano, M. Rösner, and C. E. Dreyer, Quantum embedding methods for correlated excited states of point defects: Case studies and challenges, *Physical Review B* **105**, 235104 (2022).

[26] M. Bockstedte, F. Schütz, T. Garratt, V. Ivády, and A. Gali, Ab initio description of highly correlated states in defects for realizing quantum bits, *npj Quantum Materials* **3**, 31 (2018).

[27] H. Ma, M. Govoni, and G. Galli, Quantum simulations of materials on near-term quantum computers, *npj Computational Materials* **6**, 85 (2020).

[28] H. Ma, N. Sheng, M. Govoni, and G. Galli, First-principles studies of strongly correlated states in defect spin qubits in diamond, *Physical Chemistry Chemical Physics* **22**, 25522 (2020).

[29] H. Ma, N. Sheng, M. Govoni, and G. Galli, Quantum Embedding Theory for Strongly Correlated States in Materials, *Journal of Chemical Theory and Computation* **17**, 2116 (2021).

[30] F. Aryasetiawan, M. Imada, A. Georges, G. Kotliar, S. Biermann, and A. I. Lichtenstein, Frequency-dependent local interactions and low-energy effective models from electronic structure calculations, *Physical Review B* **70**, 195104 (2004).

[31] F. Aryasetiawan, K. Karlsson, O. Jepsen, and U. Schönberger, Calculations of Hubbard U from first-principles, *Physical Review B* **74**, 125106 (2006).

[32] T. Miyake, F. Aryasetiawan, and M. Imada, *Ab Initio* procedure for constructing effective models of correlated materials with entangled band structure, *Physical Review B* **80**, 155134 (2009).

[33] E. Şaşıoğlu, C. Friedrich, and S. Blügel, Effective Coulomb interaction in transition metals from constrained random-phase approximation, *Physical Review B* **83**, 121101 (2011).

[34] E. Pavarini, E. Koch, D. Vollhardt, A. I. Lichtenstein, Institute for Advanced Simulation, German Research School for Simulation Sciences, and D. Forschungsgemeinschaft, eds., *The LDA+DMFT Approach to Strongly Correlated Materials: Lecture Notes of the Autumn School 2011 Hands-on LDA+DMFT: At Forschungszentrum Jülich, 4-7 October 2011*, Schriften Des Forschungszentrums Jülich. Reihe Modeling and Simulation No. Band 1 (Forschungszentrum Jülich, Zentralbibliothek, Verl, Jülich, 2011).

[35] A. I. Liechtenstein, V. I. Anisimov, and J. Zaanen, Density-functional theory and strong interactions: Orbital ordering in Mott-Hubbard insulators, *Physical Review B* **52**, R5467 (1995).

[36] S. Ryee and M. J. Han, The effect of double counting, spin density, and Hund interaction in the different DFT+U functionals, *Scientific Reports* **8**, 9559 (2018).

[37] N. Sheng, C. Vorwerk, M. Govoni, and G. Galli, Green's Function Formulation of Quantum Defect Embedding Theory, *Journal of Chemical Theory and Computation* **18**, 3512 (2022).

[38] E. G. C. P. Van Loon, M. Rösner, M. I. Katsnelson, and T. O. Wehling, Random phase approximation for gapped systems: Role of vertex corrections and applicability of the constrained random phase approximation, *Physical Review B* **104**, 045134 (2021).

[39] Y. Chang, E. G. C. P. Van Loon, B. Eskridge, B. Busemeyer, M. A. Morales, C. E. Dreyer, A. J. Millis, S. Zhang, T. O. Wehling, L. K. Wagner, and M. Rösner, Downfolding from ab initio to interacting model Hamiltonians: Comprehensive analysis and benchmarking of the DFT+cRPA approach, *npj Computational Materials* **10**, 129 (2024).

[40] W. M. C. Foulkes, L. Mitas, R. J. Needs, and G. Rajagopal, Quantum Monte Carlo simulations of solids, *Reviews of Modern Physics* **73**, 33 (2001).

[41] D. Alfe and M. J. Gillan, Schottky defect formation energy in MgO calculated by diffusion Monte Carlo, *Physical Review B* **71**, 220101 (2005).

[42] W. D. Parker, J. W. Wilkins, and R. G. Hennig, Accuracy of quantum Monte Carlo methods for point defects in solids, *physica status solidi (b)* **248**, 267 (2011).

[43] R. Q. Hood, P. R. C. Kent, and F. A. Reboredo, Diffusion quantum Monte Carlo study of the equation of state and point defects in aluminum, *Physical Review B* **85**, 134109 (2012).

[44] E. Ertekin, L. K. Wagner, and J. C. Grossman, Point-defect optical transitions and thermal ionization energies from quantum Monte Carlo methods: Application to the F⁻center defect in MgO, *Physical Review B* **87**, 155210 (2013).

[45] J. Yu, L. K. Wagner, and E. Ertekin, Fixed-node diffusion Monte Carlo description of nitrogen defects in zinc oxide, *Physical Review B* **95**, 075209 (2017).

[46] R. Q. Hood, P. R. C. Kent, R. J. Needs, and P. R. Briddon, Quantum Monte Carlo Study of the Optical and Diffusive Properties of the Vacancy Defect in Diamond, *Physical Review Letters* **91**, 076403 (2003).

[47] K. Saritas, W. Ming, M.-H. Du, and F. A. Reboredo, Excitation Energies of Localized Correlated Defects via Quantum Monte Carlo: A Case Study of Mn⁴⁺-Doped Phosphors, *The Journal of Physical Chemistry Letters* **10**, 67 (2019).

[48] Y. Chen, T. Jiang, H. Chen, E. Han, A. Alavi, K. Yu, E. Wang, and J. Chen, Multiconfigurational nature of electron correlation within nitrogen vacancy centers in diamond, *Physical Review B* **108**, 045111 (2023).

[49] K. A. Simula and I. Makkonen, Calculation of the energies of the multideterminant states of the nitrogen va-

cancy center in diamond with quantum Monte Carlo, *Physical Review B* **108**, 094108 (2023).

[50] W. A. Wheeler, K. G. Kleiner, and L. K. Wagner, Ensemble variational Monte Carlo for optimization of correlated excited state wave functions, *Electronic Structure* **6**, 025001 (2024).

[51] S. Sugano, Y. Tanabe, and H. Kamimura, *Multiplets of Transition-Metal Ions in Crystals*, Pure and Applied Physics, v. 33 (Academic Press, 1970).

[52] H. Masenda, D. Naidoo, K. Bharuth-Ram, H. Gunnlaugsson, K. Johnston, R. Mantovan, T. Mølholt, M. Ncube, S. Shayestehaminzadeh, H. Gíslason, G. Langouche, S. Ólafsson, and G. Weyer, Lattice sites, charge states and spin-lattice relaxation of Fe ions in ^{57}Mn + implanted GaN and AlN, *Journal of Magnetism and Magnetic Materials* **401**, 1130 (2016).

[53] Y. Jin, M. Govoni, G. Wolfowicz, S. E. Sullivan, F. J. Heremans, D. D. Awschalom, and G. Galli, Photoluminescence spectra of point defects in semiconductors: Validation of first-principles calculations, *Physical Review Materials* **5**, 084603 (2021).

[54] A. Jain, S. P. Ong, G. Hautier, W. Chen, W. D. Richards, S. Dacek, S. Cholia, D. Gunter, D. Skinner, G. Ceder, and K. A. Persson, Commentary: The Materials Project: A materials genome approach to accelerating materials innovation, *APL Materials* **1**, 011002 (2013).

[55] G. Kresse and J. Furthmüller, Efficiency of ab-initio total energy calculations for metals and semiconductors using a plane-wave basis set, *Computational Materials Science* **6**, 15 (1996).

[56] J. P. Perdew, K. Burke, and M. Ernzerhof, Generalized Gradient Approximation Made Simple, *Physical Review Letters* **77**, 3865 (1996).

[57] Q. Sun, T. C. Berkelbach, N. S. Blunt, G. H. Booth, S. Guo, Z. Li, J. Liu, J. D. McClain, E. R. Sayfutyarova, S. Sharma, S. Wouters, and G. K.-L. Chan, PySCF: The Python-based simulations of chemistry framework, *WIREs Computational Molecular Science* **8**, e1340 (2018).

[58] A. Annaberdiyev, G. Wang, C. A. Melton, M. C. Bennett, L. Shulenburger, and L. Mitas, A new generation of effective core potentials from correlated calculations: 3d transition metal series, *The Journal of Chemical Physics* **149**, 134108 (2018).

[59] L. K. Wagner and L. Mitas, Energetics and dipole moment of transition metal monoxides by quantum Monte Carlo, *The Journal of Chemical Physics* **126**, 034105 (2007).

[60] W. A. Wheeler, S. Pathak, K. G. Kleiner, S. Yuan, J. N. B. Rodrigues, C. Lorsung, K. Krongchon, Y. Chang, Y. Zhou, B. Busemeyer, K. T. Williams, A. Muñoz, C. Y. Chow, and L. K. Wagner, PyQMC : An all-Python real-space quantum Monte Carlo module in PySCF, *The Journal of Chemical Physics* **158**, 114801 (2023).

[61] J. Heyd, G. E. Scuseria, and M. Ernzerhof, Hybrid functionals based on a screened Coulomb potential, *The Journal of Chemical Physics* **118**, 8207 (2003).

[62] J. Heyd, G. E. Scuseria, and M. Ernzerhof, Erratum: “Hybrid functionals based on a screened Coulomb potential” [J. Chem. Phys. 118, 8207 (2003)], *The Journal of Chemical Physics* **124**, 219906 (2006).

[63] G. Knizia, Intrinsic Atomic Orbitals: An Unbiased Bridge between Quantum Theory and Chemical Concepts, *Journal of Chemical Theory and Computation* **9**, 4834 (2013).

[64] P. Giannozzi, O. Andreussi, T. Brumme, O. Bunau, M. Buongiorno Nardelli, M. Calandra, R. Car, C. Cavazzoni, D. Ceresoli, M. Cococcioni, N. Colonna, I. Carnimeo, A. Dal Corso, S. De Gironcoli, P. Delugas, R. A. DiStasio, A. Ferretti, A. Floris, G. Fratesi, G. Fugallo, R. Gebauer, U. Gerstmann, F. Giustino, T. Gorni, J. Jia, M. Kawamura, H.-Y. Ko, A. Kokalj, E. Küçükbenli, M. Lazzeri, M. Marsili, N. Marzari, F. Mauri, N. L. Nguyen, H.-V. Nguyen, A. Otero-de-la-Roza, L. Paulatto, S. Poncé, D. Rocca, R. Sabatini, B. Santra, M. Schlipf, A. P. Seitsonen, A. Smogunov, I. Timrov, T. Thonhauser, P. Umari, N. Vast, X. Wu, and S. Baroni, Advanced capabilities for materials modelling with Quantum ESPRESSO, *Journal of Physics: Condensed Matter* **29**, 465901 (2017).

[65] A. A. Mostofi, J. R. Yates, G. Pizzi, Y.-S. Lee, I. Souza, D. Vanderbilt, and N. Marzari, An updated version of wannier90: A tool for obtaining maximally-localised Wannier functions, *Computer Physics Communications* **185**, 2309 (2014).

[66] K. Nakamura, Y. Yoshimoto, Y. Nomura, T. Tadano, M. Kawamura, T. Kosugi, K. Yoshimi, T. Misawa, and Y. Motoyama, RESPACK: An ab initio tool for derivation of effective low-energy model of material, *Computer Physics Communications* **261**, 107781 (2021).

[67] K. Kurita, T. Misawa, K. Yoshimi, K. Ido, and T. Koretzune, Interface tool from Wannier90 to RESPACK: Wan2respack, *Computer Physics Communications* **292**, 108854 (2023).

[68] M. S. Hybertsen and S. G. Louie, Electron correlation in semiconductors and insulators: Band gaps and quasiparticle energies, *Physical Review B* **34**, 5390 (1986).

[69] J. Deslippe, G. Samsonidze, D. A. Strubbe, M. Jain, M. L. Cohen, and S. G. Louie, BerkeleyGW: A massively parallel computer package for the calculation of the quasiparticle and optical properties of materials and nanostructures, *Computer Physics Communications* **183**, 1269 (2012).

[70] J. Baur, K. Maier, M. Kunzer, U. Kaufmann, and J. Schneider, Determination of the GaN/AlN band offset via the (-/0) acceptor level of iron, *Applied Physics Letters* **65**, 2211 (1994).

[71] F. Plasser, M. Ruckenbauer, S. Mai, M. Oppel, P. Marquetand, and L. González, Efficient and Flexible Computation of Many-Electron Wave Function Overlaps, *Journal of Chemical Theory and Computation* **12**, 1207 (2016).

[72] M. E. A. Coury, S. L. Dudarev, W. M. C. Foulkes, A. P. Horsfield, P.-W. Ma, and J. S. Spencer, Hubbard-like Hamiltonians for interacting electrons in s, p, and d orbitals, *Physical Review B* **93**, 075101 (2016).

[73] O. Parcollet, M. Ferrero, T. Ayral, H. Hafermann, I. Krivenko, L. Messio, and P. Seth, TRIQS: A toolbox for research on interacting quantum systems, *Computer Physics Communications* **196**, 398 (2015).

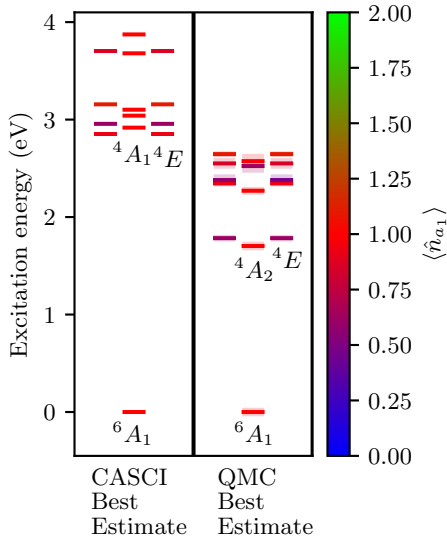


FIG. 4. Comparison of lowest vertical excitation energies between the best-estimate CASCI and best-estimate QMC calculations for the same 32-atom unit cell of $\text{Fe}_{\text{Al}}^0:\text{AlN}$.

VII. SUPPLEMENTAL INFORMATION

A. *Ab-initio* CASCI data

To show the importance of the Jastrow factor for obtaining high-accuracy *ab-initio* wave functions, we compared excitation energies between the best-estimate CASCI and the best-estimate QMC. The only difference between the CASCI and QMC is the presence of a fixed Jastrow factor. Both CASCI and QMC used the HSE06 vqz orbitals in the wave functions. As can be seen in Fig. 4, CASCI obtains lowest excitation energies 1 eV higher than with the Jastrow. The Jastrow also changes the ordering of excited states relative to CASCI, in particular switching the ordering of the lowest 4A_1 and 4A_2 states and lowering the 4E states with 0.6 occupation in the a_1 orbital.

B. Wave function irrep classification

We obtained C_{3v} spatial irrep labels for the *ab-initio* eigeneigenstates and embedding model eigenstates using expectation values of three-fold rotation \hat{C}_3 and mirror reflection $\hat{\sigma}_v$. For the QMC-computed eigenstates, expectation values of symmetry operator \hat{R} were evaluated during the Monte Carlo sampling. For the embedding model states and CASCI states discussed in Sec. VII A,

$\langle \hat{R} \rangle$ was evaluated as

$$\begin{aligned}\langle \hat{R} \rangle &= \sum_{ij} w_i w_j \left[\langle D_i^\uparrow |, \langle D_i^\downarrow | \right] \hat{R} \left[|D_j^\uparrow \rangle, |D_j^\downarrow \rangle \right] \\ &= \sum_{ij} w_i^* w_j \det[\langle \phi_{a_i}^\uparrow | \hat{R} | \phi_{b_j}^\uparrow \rangle] \det[\langle \phi_{a_i}^\downarrow | \hat{R} | \phi_{b_j}^\downarrow \rangle], \quad (6)\end{aligned}$$

where w_i is the weight on spinor determinant $[|D_i^\uparrow\rangle, |D_i^\downarrow\rangle]$ and $|\phi_{ai}^\sigma\rangle$ is one-particle orbital a in spin- σ determinant i . In deriving Eq. 6, we leveraged the proven property that the overlap of Slater determinant states is the determinant of their orbital overlaps [71]. This procedure is identical to that carried out in Ref. [25]. The irrep A_1 , A_2 , or E was then determined using the C_{3v} character table.

We obtained spin degeneracies for the irrep labels using the expectation value of \hat{S}^2 in the Fe d -like orbital basis. Using the formula derived in Ref. [72], we compute $\langle \hat{S}^2 \rangle$ as

$$\begin{aligned}
\langle \hat{S}^2 \rangle &= \sum_{i,j \in \text{Fe}_d} \hat{\mathbf{S}}_i \cdot \hat{\mathbf{S}}_j \\
&= \frac{1}{2} (N_{\text{orb}} + 2) \sum_{i \in \text{Fe}_d} \sum_{\sigma \in \{\uparrow, \downarrow\}} \langle \hat{n}_{i,\sigma} \rangle \\
&\quad - \frac{1}{2} \sum_{i,j \in \text{Fe}_d} \sum_{\sigma, \sigma' \in \{\uparrow, \downarrow\}} \langle \hat{c}_{i,\sigma}^\dagger \hat{c}_{j,\sigma} \hat{c}_{j,\sigma'}^\dagger \hat{c}_{i,\sigma'} \rangle \\
&\quad - \frac{1}{4} \sum_{i,j \in \text{Fe}_d} \sum_{\sigma, \sigma' \in \{\uparrow, \downarrow\}} \langle \hat{n}_{i,\sigma} \hat{n}_{j,\sigma'} \rangle,
\end{aligned} \tag{7}$$

where $N_{\text{orb}} = 5$ is the number of orbitals in the basis.

C. Rotations between basis sets

We obtained transformations between each Wannier basis set used for the embedding Hamiltonians and the reference IAO basis set in Fig. 1 used for the QMC density matrices. The normalized overlap matrices were computed using Riemann summation on a high-resolution 160 x 160 x 256 Cartesian grid. As can be seen in Fig. 5(a), the Wannier basis from DFT $|22100\rangle$ and the IAO basis overlap roughly 85%. Orbitals with the same cubic harmonic character overlap by roughly 96%, with some overall sign differences. The Wannier orbitals from DFT $|11111\rangle$ have similar overlaps with the IAOs. Hence, the basis transformations are not unitary. The non-unitarity likely arises from the different reference states in the underlying DFT calculations.

To determine the closest unitary transformations, we rounded the raw overlap values to +1, -1, and 0. As can be seen in Fig. 5(b), the diagonal entries in the raw transformation matrix changed by roughly 4%. The resulting transformations are a one-to-one mapping between orbitals of the same cubic harmonic character.

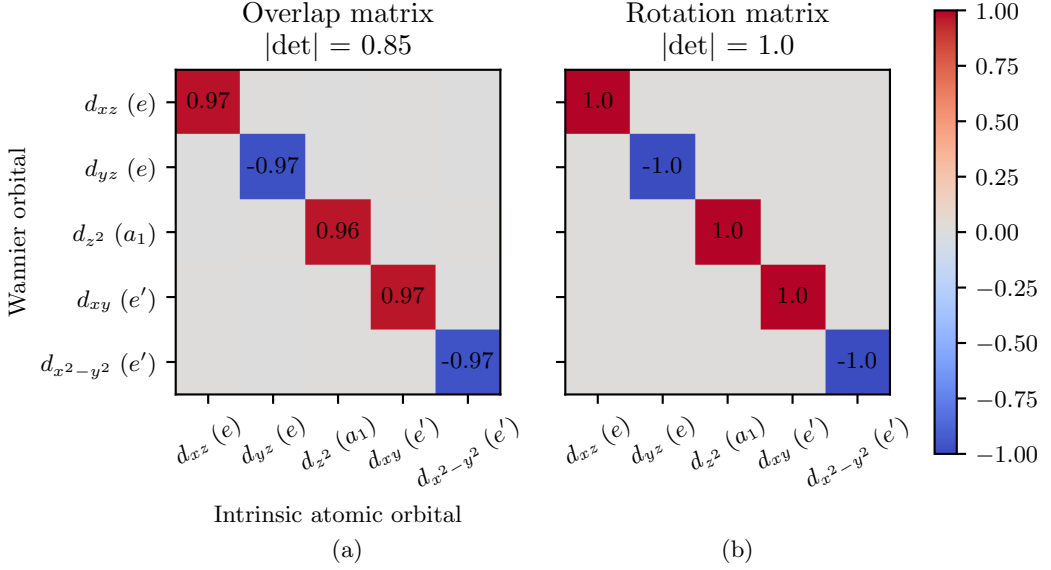


FIG. 5. Comparison of (a) raw transformation and (b) closest-unitary transformation matrices between the Wannier orbital basis from DFT $|22100\rangle$ and reference atomic orbitals in Fig. 1. Rows and columns denote the respective basis orbitals and their irreps of C_{3v} . Matrix determinants are shown at the top.

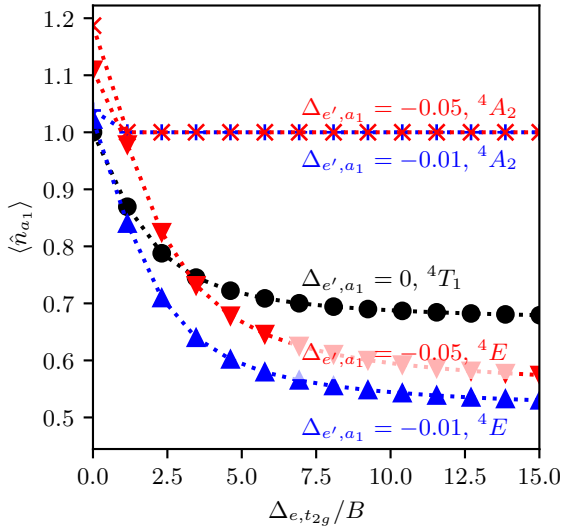


FIG. 6. Occupation in the a_1 orbital versus T_d CFS. B is the Racah parameter and $\Delta_{e,t_{2g}}/B$ and $\Delta_{a_1,e'}$ are the CFS parameters. Results for the lowest-energy many-body excited states are included, i.e., 4A_2 and 4E for C_{3v} and 4T_1 for T_d .

D. Ligand field theory for a d^5 ion in a C_{3v} field

As discussed in the main text, we carry out ligand field theory calculations to gain insight into the a_1 occupation for the excited states of $\text{Fe}_{\text{Al}}^0:\text{AlN}$. We assume a spherically symmetric form of the screened Coulomb interaction parameterized by the Slater integrals F_0 , F_2 , and F_4 [51]. The value of F_0 is not important for our

purposes since the d occupancy is fixed to five for all states of interest, and we take $F_4/F_2 = 15/23$, i.e., the value for hydrogenic d orbitals. Therefore, we are left with one free parameter, which we write as the Racah $B = (1/49)F_2 - (5/441)F_4$ [51]. We fix $B = 0.068$ eV, which is consistent with a Hund's J of 0.6 eV. The one-particle part provides the CFS of the orbitals. For the most general C_{3v} case, this matrix will be parameterized by energies of the e , a_1 and e' orbitals. We can recover T_d symmetry in our basis by setting $t_{ee'} = \sqrt{(\epsilon_{a_1} - \epsilon_e)(\epsilon_{a_1} - \epsilon_{e'})}$ and $\epsilon_{e'} = \epsilon_e/2$, which therefore has one free parameter governing the $e-t_{2g}$ splitting, which we call $\Delta_{e,t_{2g}}$. When the symmetry is lowered to C_{3v} , we have an additional parameter $\Delta_{a_1,e'}$, which governs the splitting of t_{2g} into a_1 and e' . Based on the splitting between the 4E and 4A_2 states in the QMC, we estimate $\Delta_{e,t_{2g}}/B \simeq 10$; in order to obtain the 4A_2 state slightly lower in energy than the 4E , we must choose $\Delta_{a_1,e'} < 0$, i.e., the a_1 state is lower in energy than e' .

We diagonalize this Hamiltonian using the `triqs atom_diag` tool [73]. We plot the a_1 orbital occupation taken from the diagonal elements of the one-particle density matrix for the 4E and 4A_2 states versus $\Delta_{e,t_{2g}}/B$ for different choices of $\Delta_{a_1,e'}$ in Fig. 6. Note that for $\Delta_{a_1,e'} = 0$, i.e., T_d symmetry, 4E and 4A_2 are degenerate, forming 4T_1 . We see that the qualitative behavior is relatively insensitive to the values of the CFS. $\langle \hat{n}_{a_1} \rangle = 1$ for 4A_2 for any finite $\Delta_{e,t_{2g}}$, irrespective of the value of $\Delta_{a_1,e'}$. For 4E in the range of $\Delta_{e,t_{2g}}/B$ relevant for the QMC, $\langle \hat{n}_{a_1} \rangle$ decreases from 1 to 0.5-0.7, depending on $\Delta_{a_1,e'}$. These are exactly the occupancies observed in the QMC calculation, but quite distinct from the embedding results shown in Fig. 3 in the main text. In the limit

TABLE IV. Breakdown of irreps, vertical excitation energies, and one-particle expectation values for the best-estimate QMC states.

irrep	energy (eV)	$\langle \hat{n}_e \rangle$	$\langle \hat{n}_{e'} \rangle$	$\langle \hat{n}_{a_1} \rangle$	$\langle \hat{t}_{ee'} \rangle$
6A_1	0.00(6)	1.98	1.99	0.99	0.00
4A_2	1.70(6)	2.14	1.84	1.00	1.75
4E	1.78(4)	2.52	1.84	0.61	1.10
4A_1	2.27(5)	2.20	1.78	1.00	0.12
4E	2.35(4)	2.07	1.97	0.92	0.03
2E	2.38(9)	2.57	1.80	0.58	1.63
2A_2	2.5(1)	2.51	1.82	0.63	1.12
4E	2.55(8)	2.37	1.72	0.85	0.60
2A_1	2.6(1)	2.98	2.01	0.98	1.92
4E	2.65(3)	1.98	1.90	1.09	0.08

of T_d symmetry, the 4T_1 manifold constitutes roughly a average of these occupancies for 4E and 4A_2 .

E. Detailed state data

We computed the expectation values of e orbital occupation, e' orbital occupation, a_1 orbital occupation, and

$e-e'$ hopping in all eigenstates from QMC and embedding, defined using operators in second quantization in the Fe d -like IAO basis as

$$\hat{n}_e = \sum_{\sigma \in \{\uparrow, \downarrow\}} (\hat{n}_{d_{xz}, \sigma} + \hat{n}_{d_{yz}, \sigma}), \quad (8)$$

$$\hat{n}_{e'} = \sum_{\sigma \in \{\uparrow, \downarrow\}} (\hat{n}_{d_{xy}, \sigma} + \hat{n}_{d_{x^2-y^2}, \sigma}),, \quad (9)$$

$$\hat{n}_{a_1} = \sum_{\sigma \in \{\uparrow, \downarrow\}} \hat{n}_{d_{z^2}, \sigma}, \quad (10)$$

$$\hat{t}_{ee'} = \sum_{\sigma \in \{\uparrow, \downarrow\}} (\hat{c}_{d_{xz}, \sigma}^\dagger \hat{c}_{d_{xy}, \sigma} + \hat{c}_{d_{yz}, \sigma}^\dagger \hat{c}_{d_{x^2-y^2}, \sigma} + hc). \quad (11)$$

The four quantities in Eqs. (8-11) are invariant to C_{3v} symmetry operations. We report a detailed characterization of all eigenstates in Tables IV-IX.

TABLE V. Breakdown of irreps, vertical excitation energies, and one-particle expectation values for the states from DFT+cRPA $|22100\rangle$ with Hartree DC correction.

irrep	energy (eV)	$\langle \hat{n}_e \rangle$	$\langle \hat{n}_{e'} \rangle$	$\langle \hat{n}_{a_1} \rangle$	$\langle \hat{t}_{ee} \rangle$
2A_1	0.00	2.98	1.02	1.00	3.45
2E	0.97	3.38	1.61	0.02	2.38
4A_2	2.04	1.53	1.47	1.00	1.68
4E	2.11	2.57	1.44	0.98	1.61
4A_1	2.22	1.62	1.38	1.00	1.55
2E	2.28	2.23	0.92	1.85	2.51
2A_1	2.77	2.53	1.51	0.96	1.66
2A_1	2.95	2.56	1.47	0.97	1.62
2E	3.05	2.58	1.46	0.97	1.60
2A_1	3.10	2.62	1.42	0.96	1.51

TABLE VI. Breakdown of irreps, vertical excitation energies, and one-particle expectation values for the states from DFT+cRPA $|11111\rangle$ with Hartree DC correction.

irrep	energy (eV)	$\langle \hat{n}_e \rangle$	$\langle \hat{n}_{e'} \rangle$	$\langle \hat{n}_{a_1} \rangle$	$\langle \hat{t}_{ee} \rangle$
2A_1	0.00	2.67	1.33	1.00	3.70
2E	0.05	2.35	1.73	0.02	2.50
6A_1	0.50	2.00	2.00	1.00	0.00
4A_2	0.66	2.40	1.60	1.00	1.81
4E	0.68	2.53	1.67	0.80	1.55
4A_1	0.83	2.53	1.47	1.00	1.63
4E	1.03	2.69	2.08	0.23	0.98
2A_2	1.23	2.51	1.72	0.76	1.55
2E	1.41	2.33	1.50	1.17	1.96
2A_2	1.46	2.46	1.61	0.93	1.71

TABLE VII. Breakdown of irreps, vertical excitation energies, and one-particle expectation values for the states from DFT+cRPA $|22100\rangle$ without DC correction.

irrep	energy (eV)	$\langle \hat{n}_e \rangle$	$\langle \hat{n}_{e'} \rangle$	$\langle \hat{n}_{a_1} \rangle$	$\langle \hat{t}_{ee} \rangle$
6A_1	0.00	2.00	2.00	1.00	0.00
4E	1.35	1.73	1.51	1.76	0.76
4A_1	1.53	2.11	1.89	1.00	0.00
4E	1.55	2.07	1.81	1.12	-0.06
4E	1.74	2.46	1.82	1.72	-0.72
4A_1	1.75	2.18	1.82	1.00	-0.18
4A_2	1.89	2.52	1.49	1.00	0.19
4E	1.96	2.36	1.61	1.03	0.91
4A_1	1.99	2.09	1.91	1.00	0.55
4A_2	2.00	2.94	2.06	1.00	0.34

TABLE VIII. Breakdown of irreps, vertical excitation energies, and one-particle expectation values for the states from DFT+crPA $|11111\rangle$ without DC correction.

irrep	energy (eV)	$\langle \hat{n}_e \rangle$	$\langle \hat{n}_{e'} \rangle$	$\langle \hat{n}_{a_1} \rangle$	$\langle \hat{t}_{ee'} \rangle$
6A_1	0.00	2.00	2.00	1.00	0.00
4E	1.21	1.70	1.52	1.77	0.87
4A_1	1.40	2.21	1.79	1.00	0.07
4E	1.46	2.00	1.89	1.11	0.05
4A_2	1.55	2.27	1.73	1.00	1.76
4E	1.62	2.51	1.54	0.95	1.20
4A_1	1.64	2.21	1.78	1.00	-0.14
4A_1	1.71	2.03	1.97	1.00	1.21
4E	1.78	1.76	1.75	1.49	-0.43
4A_2	1.94	2.34	1.66	1.00	-0.76

TABLE IX. Breakdown of irreps, vertical excitation energies, and one-particle expectation values for the states from G_0W_0 $|22100\rangle$ with G_0W_0 DC correction.

irrep	energy (eV)	$\langle \hat{n}_e \rangle$	$\langle \hat{n}_{e'} \rangle$	$\langle \hat{n}_{a_1} \rangle$	$\langle \hat{t}_{ee'} \rangle$
6A_1	0.00	2.00	2.00	1.00	0.00
4E	0.76	2.00	1.95	1.96	-0.15
4E	0.88	1.03	2.00	1.96	0.15
4E	1.48	2.20	1.80	1.00	-0.50
2E	1.51	1.30	1.74	1.96	-2.27
4A_1	1.53	2.14	1.86	1.00	-0.06
2E	1.63	1.33	1.73	1.94	-1.15
4A_2	1.65	2.34	1.66	1.00	-1.63
2A_2	1.66	1.30	1.81	1.89	-0.92
4A_1	1.69	2.27	1.73	1.00	-0.56